Original Article

Institution of MECHANICAL ENGINEERS

Journal of SYSTEMS AND CONTROL ENGINEERING

Proc IMechE Part I:
J Systems and Control Engineering
2021, Vol. 235(3) 330–346

DOI: 10.1177/0959651820953254
journals.sagepub.com/home/pii
SAGE

A rapid neural network–based state of health estimation scheme for screening of end of life electric vehicle batteries

Alireza Rastegarpanah[1,2]*, Jamie Hathaway[1]*, Mohamed Ahmeid[2,3], Simon Lambert[2,3], Allan Walton[1,2] and Rustam Stolkin[1,2]

Abstract

There is growing interest in recycling and re-use of electric vehicle batteries owing to their growing market share and use of high-value materials such as cobalt and nickel. To inform the subsequent applications at battery end of life, it is necessary to quantify their state of health. This study proposes an estimation scheme for the state of health of high-power lithium-ion batteries based on extraction of parameters from impedance data of 13 Nissan Leaf 2011 battery modules modelled by a modified Randles equivalent circuit model. Using the extracted parameters as predictors for the state of health, a baseline single hidden layer neural network was evaluated by root mean square and peak state of health prediction errors and refined using a Gaussian process optimisation procedure. The optimised neural network predicted state of health with a root mean square error of $(1.729 \pm 0.147)\%$, which is shown to be competitive with some of the most performant existing neural network–based state of health estimation schemes, and is expected to outperform the baseline model with $\sim$50 training samples. The use of equivalent circuit model parameters enables more in-depth analysis of the battery degradation state than many similar neural network–based schemes while maintaining similar accuracy despite a reduced dataset, while there is demonstrated potential for measurement times to be reduced to as little as 30 s with frequency targeting of the impedance measurements.

Keywords
Neural networks, electric vehicles, state of health, lithium-ion batteries, screening, gateway testing

Date received: 6 May 2020; accepted: 30 July 2020

Introduction

Recent years have seen a rapid increase in the number of electric vehicles (EVs) in circulation.[1] Owing to the use of high-value materials, such as cobalt and nickel, there is a strong economic, environmental and political case to implement solutions for recycling and re-use end of life EV batteries based on lithium-ion technology.[1–3] Such batteries have, for the most part, exhausted their useful life for re-use in EVs, however have demonstrably useful applications in repurposed static energy storage systems and represent a large body of energy storage capacity.[1,4] It is necessary, however, to properly assess the battery condition and degradation to inform the appropriate re-use applications or, if necessary, subsequent recycling.[3] The re-use of batteries for a second life application presents a further requirement to properly match batteries of similar condition in a given energy storage system to prevent unbalanced degradation by over (dis-)charging,[4,5] which can reduce its remaining useful life (RUL).

A quantity of particular interest for characterisation of batteries is the battery state of health (SoH), typically defined from measurements of the battery capacity for

---

[1] Department of Metallurgy and Materials Science, University of Birmingham, Birmingham, UK
[2] The Faraday Institution, Quad One, Harwell Science and Innovation Campus, Didcot, UK
[3] School of Electrical Engineering, Newcastle University, Newcastle upon Tyne, UK

*Rastegarpanah and Hathaway are identified as joint lead authors of this work.

Corresponding author:
Alireza Rastegarpanah, Department of Metallurgy and Materials Science, University of Birmingham, Edgbaston, Birmingham B15 2TT, UK.
Email: a_r_adrex@yahoo.com

lithium-ion batteries (LIBs). Typically cells with greater than 80% of their rated capacity are considered for re-use in EV applications,[4–6] while below this threshold, cells with as little as 65% of their original capacity are suitable for second-life applications. Currently, cell capacity is determined by discharge testing which takes several hours, making it a time consuming, and hence costly process.[7] Electrochemical impedance spectroscopy (EIS) is a promising technique that provides insight into the battery condition through exposing the changes in parameters pertaining to the battery internal resistance and electrochemical properties, and has presented considerable improvements in measurement times. These qualities justify its extensive prior applications in investigation of battery condition[8–11] and SoH.[12,13] It has been demonstrated through equivalent circuit (EC) modelling of the impedance response of cells that the charge transfer resistance extracted from EIS measurements is a useful indicator of SoH[13]; however, a principal limitation is that individually such parameters do not always vary significantly or linearly with the battery age,[14] and therefore it is suggested that these approaches are inadequate for SoH estimation in this case.

Recent years have seen exploration of numerous machine learning schemes to estimate SoH.[12,15–18] Neural networks (NNs) in particular are an attractive solution to SoH estimation in that they can model complex, non-linear systems with cross-interactions between system variables without a detailed underlying theoretical framework of the system being considered.[12] This is useful for LIBs where the precise internal composition and design is often commercially sensitive and hence not accessible. Nonetheless, to the authors' best knowledge, very few prior works have developed an NN-based SoH estimation scheme using such extracted parameters directly from EIS as predictors for the SoH.

In this study, an NN-based approach for estimation of the SoH from impedance measurements of Nissan Leaf 2011 battery modules is presented. This study aims to replicate the successes of prior, high-accuracy NN-based approaches, while addressing their primary limitations, namely, model complexity, large required training dataset size and lack of physical parameters extracted that pertain to the battery condition. Hence, the expected contributions of this work are as follows:

- High-accuracy estimation of SoH with a reduced training dataset of 106 samples, with an average estimation error below 3%.
- Consideration of parallel battery arrangements in contrast to focus on single cell SoH estimation in similar studies.
- The proposal of an optimised equivalent circuit model (ECM) parameter-based NN model using hyperparameter optimisation, which is not explicitly considered in most works.
- Greater insight into the battery degradation due to use of an ECM approach than available with schemes monitoring evolution of battery current/voltage.

Background and related works

The problem of state measurement of LIBs has been widely studied, most notably for estimation of the battery state of charge (SoC), while literature pertaining to SoH estimation remains less prevalent. Focuses of recent works in the area of SoH estimation have included incremental capacity (IC)/differential voltage (DV) measurement,[19] Coulomb counting,[20] (dual) extended Kalman filters[21,22] or empirical health degradation models such as those developed by Perez et al.[23] However, the bulk of literature pertaining to SoH estimation focuses on prognostics and health management of existing battery systems,[24] with less emphasis placed on end of life characterisation of batteries. Furthermore, a majority of SoH estimation works focus on single cells. This presents a problem in the EV application, where cells are often built up in parallel to form battery modules. In Chang et al.,[25] the problem of capacity estimation of parallel battery arrangements based on discharge current curves was studied, with the benefit of being validated across multiple cell chemistries. However, although this approach effectively reduced measurement times by the requirement for only a single discharge cycle, this does not eliminate the requirement to perform a discharge test entirely.

EIS

EIS represents an advanced characterisation tool for investigation of the ageing state of batteries. Studies of LIBs using EIS are various, with applications including quality control,[26] investigation of battery ageing mechanisms[11,27–29] and estimation of battery SoC and SoH.[13,30] The principle of operation of EIS is to sample the impedance of a cell at a range of discrete frequencies by applying a probing periodic voltage (potentiostatic) or current (galvanostatic) signal,[26] measuring the voltage or current response of the cell across a working electrode and calculating the impedance Z based on the current $\hat{I}$ and voltage phasors $\hat{V}$ as

$$Z = \frac{\hat{V}}{\hat{I}} = \frac{V_{max}}{I_{max} e^{-j\varphi}} = |Z| e^{j\varphi} \tag{1}$$

given the maximum current and voltage I_{max}, V_{max} and the phase of the current with respect to the voltage φ. EIS data are presented by Nyquist plot, for which an example idealised spectrum is shown in Figure 1. Two main approaches have been employed to extract information regarding the battery state by modelling the impedance response. The former uses detailed mathematical models, such as those by Xie et al.[31] and Liu and Zhu[32] which provide an in-depth overview of the internal condition of LIBs but require prior knowledge of the internal battery chemistry and geometry at a level which is difficult to obtain for commercial cells.

The latter, EC modelling, presents a simple, yet effective picture of the battery condition by considering the structure of the battery impedance response,

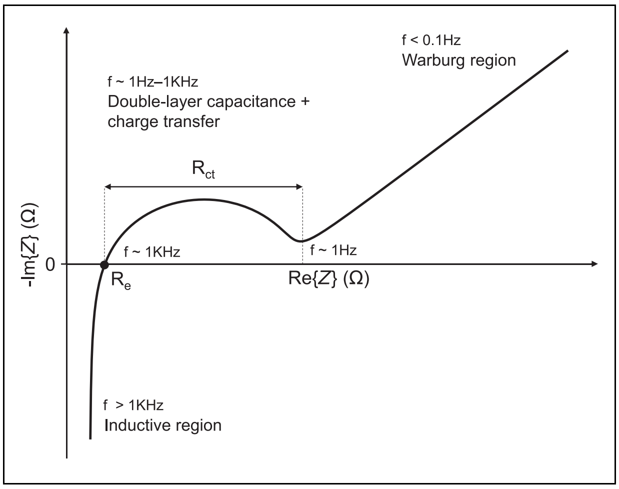

Figure 1. Idealised EIS Nyquist plot for a lithium-ion cell. The different loss mechanisms, high to low frequency (left to right) are inductive, resistive, capacitive and diffusional (Warburg impedance).

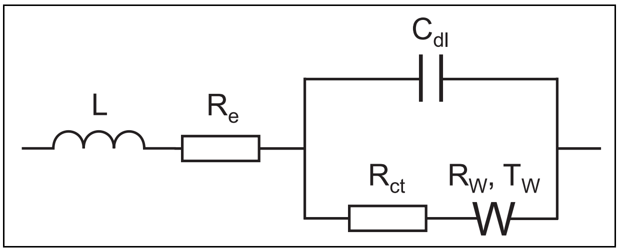

Figure 2. The Randles cell equivalent circuit model (modified with an inductor to match Figure 1), comprising a pair of resistors R_e, R_{ct}, accounting for the resistance of the electrolyte and current collector foils, capacitor C_{dl} for charge transfer effects and electrical double-layers, and a Warburg impedance Z_W element representing diffusion.[35]

defined by the internal electrical and kinetic processes occurring within the cell and associating these with one or more elements in an EC describing the system. A simple ECM for LIBs is the Randles cell (Figure 2), comprising a resistor R_e, the equivalent series resistance, accounting for the pure ohmic resistance of the electrodes, electrolyte, connecting wires and current collector foils, a resistor R_{ct} and capacitor C_{dl} to model the effects of electrical double-layers and charge transfer reactions near the electrodes and a generalised element '*W*' known as the Warburg impedance. The definition of the Warburg impedance arises from a Fick's law model of the mass transport of charged species within the electrodes and hence models the diffusion dominated low-frequency response of the cell.[33,34] The Warburg impedance under the assumption of semi-infinite diffusion is defined as

$$Z_W = \frac{R_W}{(j\omega\tau_W)^{1/2}} \tag{2}$$

where R_W is the Warburg resistance and τ_W is the Warburg time constant, defined as l^2/D, with effective diffusion thickness l and solid diffusion coefficient in the electrode material D.[13] In real cells, the thickness of the diffusion layer is often limited, motivating the so-called finite length Warburg (FLW) impedance

$$Z_{FLW} = Z_W \tanh\left((j\omega\tau_W)^{1/2}\right) \tag{3}$$

For SoH estimation with EIS, a principal issue is the limitation that results depend not only on the cell ageing state, but also on the cell's SoC, temperature and even the nature of the electrical connection between the cell and measurement equipment,[6,30,36] making reproduction of results difficult. Quantification or removal of these dependencies has been the focus of numerous works, including investigations of cells at 0% SoC,[33] while a combined study of the variation of the impedance characteristics of LIBs with temperature, SoC and ageing with EIS was first carried out by Waag et al.[9] This is more comprehensively addressed by Wang et al.,[13] leveraging this to develop an estimation function for the SoH of a lithium iron phosphate (LFP) cell based on a linear regression of the charge transfer resistance (R_{ct}) extracted by EC modelling. Such methods are advantageous in their simplicity and low computational complexity, however are limited by findings of other authors, such as Leng et al.,[14] who determined that R_{ct} changed minimally and non-linearly over ~1000 cycles for an NMC622 cell. This would suggest the variation of such parameters with battery degradation is complex, potentially non-linear and variant between differing cell chemistries and cycling histories, while it has been stressed[17] that estimating the SoH based solely on these parameters does not capture all of the relevant effects of degradation, leading to limited prediction accuracy. Eliminating other factors, such as the temperature dependence, requires either careful control of temperature in ambient chambers, as with[13,34] or correcting for with the use of data libraries[26] or by converting results to a standard reference state.[13] The latter techniques ultimately require a less sophisticated measurement setup, although require the support of large data libraries to produce self-consistent results. Such requirements present a principal motivation for the choice of a machine learning approach to leverage such data libraries to learn and account for these dependencies.

Machine learning for SoH estimation

Data-driven approaches such as machine learning have been widely studied for the development of prognostic, health management and health estimation models for a range of systems. For example, data-driven approaches have been applied with success in the related area of bearing fault diagnosis and prognostics,[37,38] where it is often impractical to develop precise health degradation models to predict their RUL. Similarly for studies of LIBs, a number of data-driven estimation models for the battery SoC,[15,39,40] SoH[12,15–18,41] and RUL have been developed.[12,42,43] Many of these studies focus on online estimation of SoH by capacity, with the prevailing approach involving following the evolution of the current, terminal voltage and partial capacity curves of the battery with time as applied by previous works.[17,18,43] These approaches have the potential to provide rapid SoH estimation; for example,[17] applied an artificial neural network (ANN)-based classifier on features extracted from fixed time windows of as little as 60 s. In the case of Bonfitto et al.,[17] this is achieved with low computational complexity; however, a limitation is that it is based on classification into discrete SoH bands of 5% and hence is limited in precision. On the other hand, Shen et al.[18] used deep convolutional neural networks (DCNNs) with transfer and ensemble learning with demonstrably high accuracy and precision, but with greatly increased computational complexity.

Other models based on recurrent neural networks (RNNs) focus on time series forecasting of the battery state. Such an approach is applied in Eddahech et al.[12] monitors the degradation of capacity and internal resistance with time to develop a high-accuracy SoH degradation model. More recently, similar approaches have been explored based on the RNN principle by monitoring the cell current and terminal voltage, including application of the gated recurrent unit (GRU) RNN by Jiao et al.[39] and long short-term memory (LSTM) in Mamo and Wang[40] for the related problem of SoC estimation, as well as a modified LSTM in Li et al.[43] for estimation of SoH. Generally, the RNN-based approaches are capable of predicting the battery states with outstanding accuracy and can be extended in the case of SoH to predict the evolution of the battery condition for estimation of RUL as in Eddahech et al.[12] and Li et al.[43] However, being suited for state monitoring, a key limitation is the sensitivity of model predictions to the previous battery state, which makes these approaches unsuitable for characterisation of most end of life batteries.

For non-RNN-based approaches, typical root mean square (RMS) prediction errors for NNs range between 1% and 5%, while some approaches such as those by Kim et al.[41] and Liu et al.[44] are shown to achieve even greater capacity prediction performance. The high prediction accuracy is achieved based on application of highly complex NN models, with the caveat that as the number of neurons used to model the system increases, there is a larger requirement for training data to prevent over-fitting of the network to the training dataset, while the model becomes more computationally demanding due to the increased number of model parameters.[17]

Most critically, it has been noted[6] that a principal limitation of many of these NN studies is the lack of detailed information regarding the battery ageing state, such as that exposed by the extraction of ECM parameters from EIS. Few approaches have been explored with an NN-based scheme to estimate cell SoH directly using ECM parameters, with prior studies proposing an extreme learning machine (ELM) monitoring the evolution of ECM parameters as SoH predictors with cell cycling[15] or a single hidden layer feed-forward NN[16] based on ECM parameters extracted with hybrid pulse-power characterisation (HPPC). The accuracies for these approaches lie with RMS prediction errors between 2.4% and 5%, ultimately suggesting there is scope for further study and improvement in this area. Beyond the ECM approach to battery modelling, more generalised approaches such as fuzzy c-regression have been introduced for parameter estimation of non-linear systems by Jabeur Telmoudi et al.[45] and later extended to modelling batteries in Telmoudi et al.[46] in which a fuzzy c-regression model with Euclidean particle swarm optimisation is employed to build a model of an NiMH battery under cycling, which is used to estimate SoH with high accuracy. However, although such methods are capable of modelling the battery behaviour with potentially higher accuracy than an ECM-based approach, it is unclear how these parameters are related to physical degradation phenomena occurring within the cell.

Data library

A library of impedance spectra and corresponding discharge capacities was used for the present study, measured from a series of 13 battery modules from an end of life Nissan Leaf 2011 battery pack to obtain a realistic representation of the end of life battery condition. Each module is arranged in a 2P-2S configuration with three terminals – red, white and black – with each parallel arrangement of two cells accessible by measurement across the red and white and black and white terminals, respectively. For each parallel arrangement of cells, occupying a combined capacity range of 50–55.5 A h (77%–85% SoH) impedance data were collected at room temperature (25 °C), sampling the module impedance over a logarithmically spaced frequency range of 1 kHz–15 mHz at six points per decade (30 total). This was performed at a range of SoCs from 20% to 100% SoC in intervals of 20% SoC, generating a total of 128 impedance spectra (Figure 3).

Methodology

The present work aims to develop an NN model of the SoH of end of first life EV batteries by estimation of the discharge capacity. This is proposed based on their impedance characteristic measured by impedance spectroscopy, from which physical parameters pertaining to the battery condition may be extracted by fitting to an ECM. In this case, the SoH was considered to be the ratio of the battery discharge capacity to the original rated battery capacity, as this forms the basis of typical screening criteria for end of life batteries. Using these

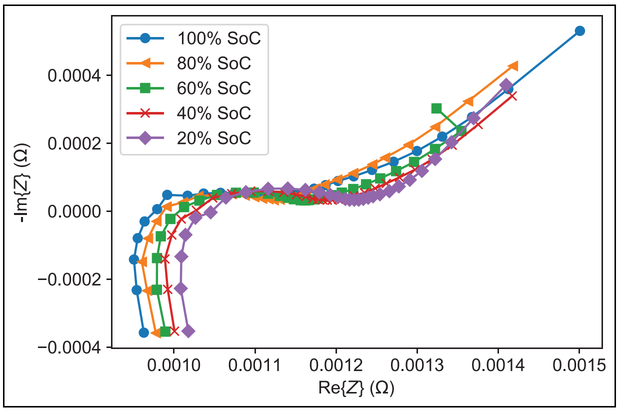

Figure 3. Experimental impedance data obtained at 25 °C, frequency range 1 kHz–15 mHz over the red and white terminals of module 1 of 13, capacity 54.9 A h and variation with battery state of charge (SoC).

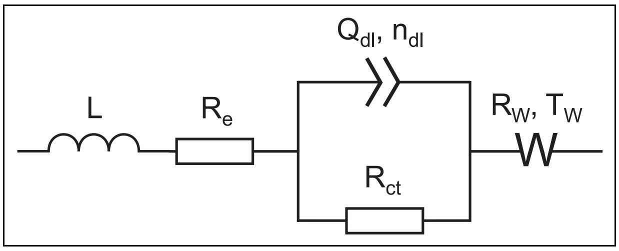

Figure 4. Diagram of the modified Randles circuit used as an equivalent circuit model (ECM) to describe the impedance response of the cells used in this study. The ECM parameters associated with each element are listed, respectively.

Table 1. Initial values of equivalent circuit model parameters for the circuit shown in Figure 3 for fitting of impedance data for all cell arrangements considered.

Fitting parameter	Initial value	Unit
R_e	–	Ω
R_{ct}	–	Ω
Q_{dl}	75	Ω^{-1} $s^{n_{dl}}$
n_{dl}	0.8	
R_W	6×10^{-4}	Ω
τ_W	5	s
L	6×10^{-8}	H

R_e and R_{ct} were directly estimated from the Nyquist representation of the impedance data.

parameters, a simple baseline model with low computational complexity is first proposed to estimate SoH before the arguments and methodology for refining the model to increase accuracy are presented.

Parameter extraction

As previously mentioned, NNs are excellent at learning the behaviour of non-linear systems, cross-interaction between system variables and existing patterns in the data used to train the network. While this is the case, it often requires large amount of data to learn general patterns in the data to generalise well to new problems. Since the goal of this study is to work with a dataset smaller than considered in other studies, it is necessary to extract features from the dataset that have a well-defined relation to the desired output (SoH). An ECM-based method for parameter extraction fits this problem well due to the well-documented relationship between the equivalent series and charge transfer resistances (R_e, R_{ct}) of the cell, as well as the Warburg resistance R_W. In this case, using the Randles circuit in Figure 2 as a baseline, a modified Randles circuit (Figure 4) is proposed to fit the data, with an inductor to model the inductance **L** of the connecting measurement leads that dominates the impedance response at high frequencies, while the capacitor modelling double-layer effects were replaced with a constant phase element owing to the potentially non-ideal capacitive behaviour of electrical double-layers at the cell electrode–electrolyte interface. The constant phase element impedance is defined as[30,35]

$$Z_{CPE} = \frac{1}{(j\omega)^n Q} \tag{4}$$

where the capacitance C_{dl} is replaced with a generic quantity Q_{dl} known as a phasance (units Ω^{-1} s^n), with exponent $0 \leqslant n \leqslant 1$ describing deviations from ideal capacitive behaviour, with $n = 0$, $n = 1$ corresponding to a pure resistor and capacitor, respectively. The impedance of the circuit can thus be described as

$$Z = R_e + j\omega L + \frac{R_W \tanh(\sqrt{j\omega\tau_W})}{\sqrt{j\omega\tau_W}} + \frac{R_{ct}}{R_{ct}Q_{dl}(j\omega)^{n_{dl}} + 1} \tag{5}$$

where R_e, R_{ct}, Q_{dl}, n_{dl}, R_W, τ_W and L constitute the free ECM fitting parameters. Fitting was performed using the Levenberg–Marquardt non-linear least squares fitting algorithm using the LMFit Python library.[47] For the fitting algorithm, initial estimates for R_e and R_{ct} were extracted directly from the impedance data as the value of $\mathrm{Re}\{Z\}$ assumed at the $-\mathrm{Im}\{Z\} = 0$ intersection and diameter of the double-layer capacitance loop, respectively. The remaining parameters were estimated using a manual search informed by parameter ranges extracted from Wang et al.[13] (see Table 1).

The SoH ground truth values were then taken to be the ratio of the measured discharge capacity q_d of each battery arrangement to its rated (nominal) capacity q_n as

$$\mathrm{SoH} = \frac{q_d}{q_n} \tag{6}$$

where q_n for a battery module as quoted by the manufacturer was 65 A h.

Baseline model

To estimate the SoH of the cells using the extracted parameters, a feed-forward NN approach is proposed

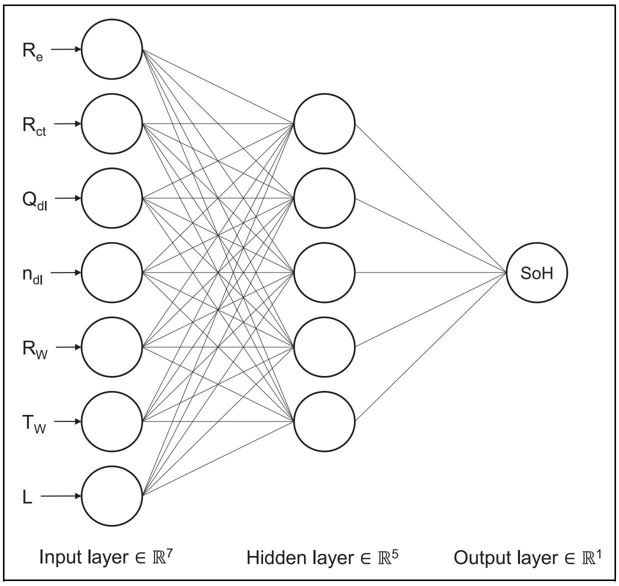

Figure 5. Diagram of the baseline feed-forward neural network architecture using extracted equivalent circuit model parameters as predictors for the battery state of health.

as a baseline method as shown in Figure 5. Development and training of the NN model was performed in Python using the publicly available machine learning libraries Keras and TensorFlow 2[48] on an NVIDIA GTX 1060 6-GB GPU using the Adam[49] optimiser. The model weights were initialised with a Glorot uniform scheme, with the sigmoid hidden layer activation function, an optimiser learning rate of 0.01 and no output layer activation function. To test the accuracy of the NN model, the dataset was partitioned according to a K-fold cross-validation scheme. K-fold cross-validation is a commonly used technique to achieve more reliable indicators of NN performance with smaller datasets[50,51] and involves shuffling the dataset prior to splitting into K equal partitions, or folds. Typically $K-1$ folds are used to train the NN model while the remaining fold is held out as a previously unseen testing dataset. The model is then evaluated K times by chosen metrics based on its performance on the test fold. After each repetition, the training and test folds are cyclically permuted such that every fold is held out as a test fold at least once. A value of $K=6$ was chosen for this study as a balance between validation accuracy and training performance and was evaluated by RMS, mean absolute (MA) and peak prediction errors defined as

$$\mathrm{RMSE} = \sqrt{\frac{1}{P}\sum_{p=0}^{P}\left(Y_p - y_p\right)^2} \tag{7}$$

$$\mathrm{MAE} = \frac{1}{P}\sum_{p=0}^{P}\left|Y_p - y_p\right| \tag{8}$$

for each SoH value p with prediction y_p and ground truth value Y_p over all predictions P. To improve the training performance owing to the disparate numeric scales of the input parameters, each input variable X in the dataset was normalised using the following scheme

$$X_{norm} = \frac{X - \bar{X}_{train}}{\sigma_{X,\,train}} \tag{9}$$

while the SoH ground truth values were normalised as

$$\mathrm{SoH}_{norm} = \frac{\mathrm{SoH} - \mathrm{SoH}_{train,\,min}}{\mathrm{SoH}_{train,\,max} - \mathrm{SoH}_{train,\,min}} \tag{10}$$

where $\bar{X}_{train}$, $\sigma_{X,\,train}$, $SoH_{train,\,min}$, $SoH_{train,\,max}$ are the mean, standard deviation, minimum and maximum values of their respective variables, calculated from the training folds only, and are applied to both the training and test folds independently. Finally, during training, an early stopping callback was used that halts the training process when no average improvement in validation error on the test set is found over the last 30 passes over the full training dataset (training epochs).

NN optimisation

It is well documented that to achieve the best NN prediction performance for a given problem, it is necessary to consider the choice of so-called network ‘hyperparameters’. For a given model, the hyperparameters include the number of neurons present in each hidden layer, the number of hidden layers and the ‘learning rate’ of the optimiser used to control the magnitude of updates to the network weights and biases. Over-fitting to the training data is a critical problem when dealing with small datasets, so it is necessary to find a balance between developing a model that is sufficiently complex to find generalised patterns in the data, such that it generalises well to an unseen dataset, and limiting over-fitting by preventing the network from adapting to patterns specific to the training data, such as noise, thus hampering its generalising power. To achieve this, the full dataset was first split into six folds as previously with a single fold held out for testing, the remaining folds forming an ‘inner’ dataset. A Gaussian process (GP) optimisation algorithm introduced by Pedregosa et al.[52] was used to minimise a cost function, which in this case is the associated RMS prediction error from a fivefold cross-validation process on the five ‘inner’ folds. This cost function was evaluated with respect to the chosen hyperparameter combination in a search space detailed in Table 2. Many of the hyperparameters are self-explanatory; however, in this case, a categorical hyperparameter was included describing the NN shape. The shape controls the number of neurons in each hidden layer based on the number of neurons in the first hidden layer. For the ‘funnel’ structure, the number of neurons in the kth hidden layer N_k is

$$N_k = N_0 - \frac{(N_0 - N_{out})}{K}k \tag{11}$$

Table 2. The hyperparameter search space used to optimise the neural network performance.

Hyperparameter	Range	Sampling
Hidden activation function	tanh, sigmoid, ReLU, ELU	Uniform
First hidden layer neurons	3–50	Uniform
Hidden layers	1–5	Uniform
Optimiser learning rate	0.01–0.5	Log-uniform
Network shape	Funnel, brick	Uniform
L2 regularisation	0–0.01	Uniform
Hidden layer dropout	0–0.3	Uniform

ELU: exponential linear unit; ReLU: rectified linear unit.

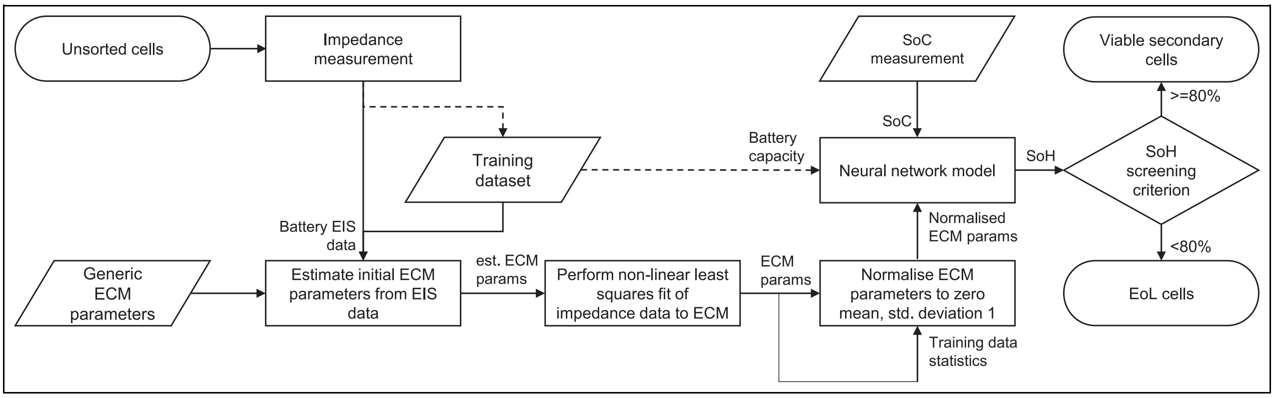

Figure 6. Block diagram of the overall SoH estimation procedure using the proposed neural network model.

rounded to the nearest integer (half to even) where N_0 is the number of neurons in the first hidden layer, N_{out} is the number of output neurons and K is the number of hidden layers. For the 'brick' structure

$$N_k = N_0 \tag{12}$$

The hidden layer dropout hyperparameter represents the fraction of neuron outputs from each layer that are set to zero during the training process to prevent overfitting.

For the GP estimator for the cost function, the Matérn covariance function was used, defined as

$$k(x_i, x_j) = \frac{2^{1-\nu}}{\Gamma(\nu)}\left(\sqrt{2\nu}\frac{d(x_i, x_j)}{\rho}\right)^{\nu} K_\nu\left(\sqrt{2\nu}\frac{d(x_i, x_j)}{\rho}\right) \tag{13}$$

with Γ as the gamma function, $K_\nu(\dots)$ as the modified Bessel function of the second kind, $d(x_i, x_j)$ as the Euclidean distance between two given points x_i and x_j, and ρ as the kernel length scale. ν is taken to be 5/2. During each optimisation run, the cost function was first evaluated a total of 250 times with hyperparameters randomly sampled according to the sampling scheme in Table 2 to generate a surrogate posterior function estimating the cost function with respect to the hyperparameter search space.

This surrogate function was used to guide 250 additional evaluations of the cost function by evaluating at the point with the minimum negative expected improvement, probability of improvement and lower confidence bound acquisition functions. In this way, convergence to the model with the lowest prediction error is achieved much more rapidly than the simpler random search or grid search of hyperparameters. Once the optimal cost function was found, a new model was generated with the resulting hyperparameters and evaluated on the held-out sixth test fold. This process was repeated six times for all six original folds. Finally, the combination of hyperparameters that achieved the lowest RMS prediction error on its test set was chosen to generate the final NN model used to estimate SoH for this study. Once the optimised model has been generated, the overall SoH estimation procedure based on the resulting SoH model is shown in Figure 6.

Results and discussion

To evaluate the effectiveness of this SoH estimation scheme, the results of the parameter extraction method, hyperparameter optimisation and comparison with the baseline model are presented here. The proposed SoH estimation scheme is compared with a range of alternative machine learning schemes, including commonly used techniques as well as approaches specific to similar studies addressed in the related works. Finally, the performance of the scheme is assessed in the context of reducing measurement times by considering the model performance on a reduced frequency range dataset.

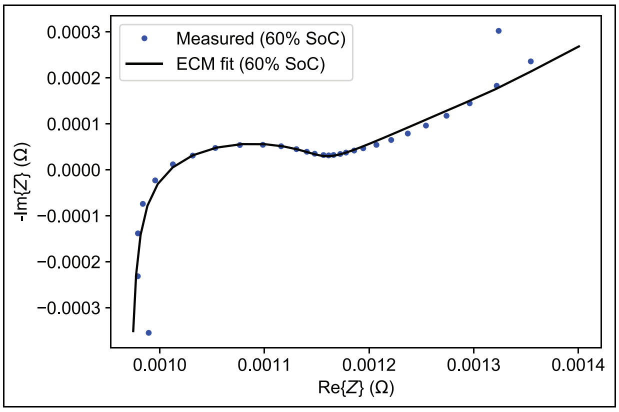

Figure 7. Nyquist plot of fit to equivalent circuit model shown in Figure 4 with experimental impedance data obtained at 60% SoC, 25 °C, frequency range 1 kHz–15 mHz over the red and white terminals of module 1 of 13, capacity 54.9 A h.

Table 3. Fitted values of equivalent circuit model (ECM) parameters corresponding to the ECM fit presented in Figure 7.

Fit parameter	Value	Unit
R_e	$9.69 \times 10^{-4} \pm 6.85 \times 10^{-6}$	Ω
R_{ct}	$1.77 \times 10^{-4} \pm 8.81 \times 10^{-6}$	Ω
Q_{dl}	35.3 ± 8.33	$\Omega^{-1}\ s^{n_{dl}}$
n_{dl}	0.852 ± 0.0480	–
R_W	$1.08 \times 10^{-3} \pm 2.61 \times 10^{-4}$	Ω
τ_W	92.5 ± 41.4	s
L	$5.84 \times 10^{-8} \pm 1.35 \times 10^{-9}$	H

ECM fit

Figure 7 shows an impedance spectrum from the dataset considered in this study over the red and white terminals of module 1 of 13 with capacity 54.9 A h, obtained at 60% SoC, 25 °C over the frequency range 1 kHz–15 mHz. This has been fitted to the modified Randles circuit in Figure 4 with the resulting fitted parameters presented in Table 3. Here, the form of the ECM used is justified by the presence of a capacitive loop present in the medium frequency range, which was attributed to be due to the double-layer capacitance and charge transfer reactions at the electrodes. A deviation from ideal capacitive behaviour is observed in the depression of the loop and slight shift of high-frequency phase away from 90°[35] and hence justifies the substitution of the double-layer capacitance in the Randles circuit for a constant phase element describing this deviation from ideality.[30,35] The presence of a tail on the spectrum at high frequencies reaching into the positive imaginary range is indicative of inductive behaviour. Finally, at low frequencies, the characteristic Warburg region is observed. The ECM used is shown to fit well to the capacitive region of the spectrum; however, deviations from the expected Warburg behaviour are observed at low frequencies. The fit could be improved by inclusion of further ECM elements; however, this complicates the fitting process by introducing greater uncertainty of the values of the fitting parameters due to the low information content of the impedance spectrum.[27]

Hyperparameter optimisation

As previously discussed, it is necessary to consider the hyperparameters of a given NN model to achieve the best accuracy. Figure 8 shows the results of the hyperparameter search, with the partial dependence of the RMS prediction error with respect to each hyperparameter shown on the diagonal, and contour plots of the partial dependence surface over each pair of hyperparameter values, which show higher and lower prediction errors in the darkened (blue) and pale (yellow) regions, respectively. The partial dependence plots between two hyperparameters were computed by evaluating the surrogate function 250 times at 40 points in hyperparameter space with all other hyperparameters chosen randomly. The average result of this process is computed, such that the dependency plots represent the average behaviour of the cost function as any given two hyperparameters are varied. The black points for a given combination of hyperparameters correspond to a full evaluation of the cost function, with the found optimal model represented by the pale (red) point.

As shown, there is very little dependence of the network performance on average with each hyperparameter individually, with most of the dependency information encoded in the cross-interactions of different hyperparameters. When considered with other hyperparameters, there is a bias towards low, but nonzero learning rates as expected, with the optimum around 0.1 as a balance between convergence speed and stability, while the cost function is shown to slightly decrease for models with high numbers of hidden layers and models with the ‘brick’ structure as the amount of L2 regularisation penalty is increased. On a superficial level, there is a bias towards models with fewer hidden layers when considered with most hyperparameters, suggesting models of high complexity are ineffective at accurately predicting SoH with the size of dataset considered. However, a large number of cost function evaluations guided by the surrogate function were focused on models with around 17 hidden layer neurons, 3–5 hidden layers with the exponential linear unit (ELU) activation function. Furthermore, the location of the optimum of the cost function in hyperparameter search space was found to significantly diverge from that used for the baseline model, highlighting the deficiency of the simpler baseline model for this problem.

The resulting optimised NN structure is shown in Figure 9 with corresponding hyperparameters in Table 4. In this case, the model achieved an RMS fivefold cross-validation error of 1.630% on the ‘inner’ validation dataset, and 1.733% on the single held-out test fold. It is demonstrated that the model structure is significantly enlarged, with quadruple the number of hidden layers in spite of the small dataset size used, which

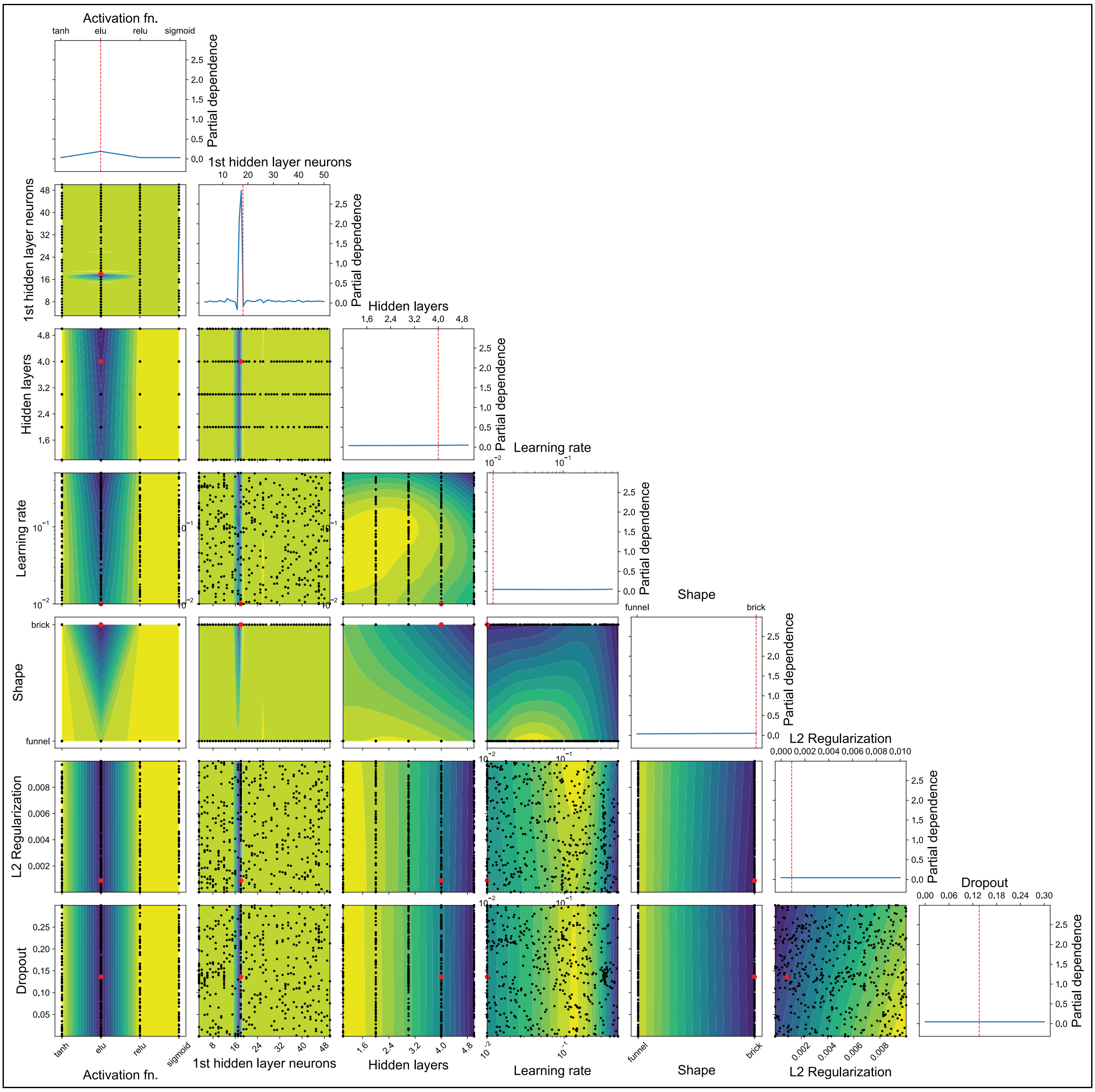

Figure 8. Result of hyperparameter optimisation showing partial dependence of RMS prediction error with each hyperparameter. Each point represents the average over a sixfold cross-validation trial of the neural network generated with the corresponding hyperparameters.

is divergent from the approaches applied by Densmore and Hanif[15] and Yang et al.[16] based on ECM parameters. For the optimised NN model, the convergence during training to a minimum mean squared prediction error was recorded over the number of training epochs for the training and validation dataset partitions, and is presented in Figure 10. The model shows rapid convergence in the first 50 epochs, with little reduction in validation error over ~350 epochs before early stopping at ~380 epochs. The training and validation errors in this case are well matched and show little to no divergence over continued training, while the inverse is widely recognised as an indicator of model over-fitting.[51]

Table 4. The optimised neural network hyperparameters corresponding to the network structure in Figure 9.

Hyperparameter	Value
Hidden activation function	ELU
First hidden layer neurons	18
Hidden layers	4
Optimiser learning rate	0.01
Network shape	Brick
L2 regularisation	0.00089
Hidden layer dropout	0.136

ELU: exponential linear unit.

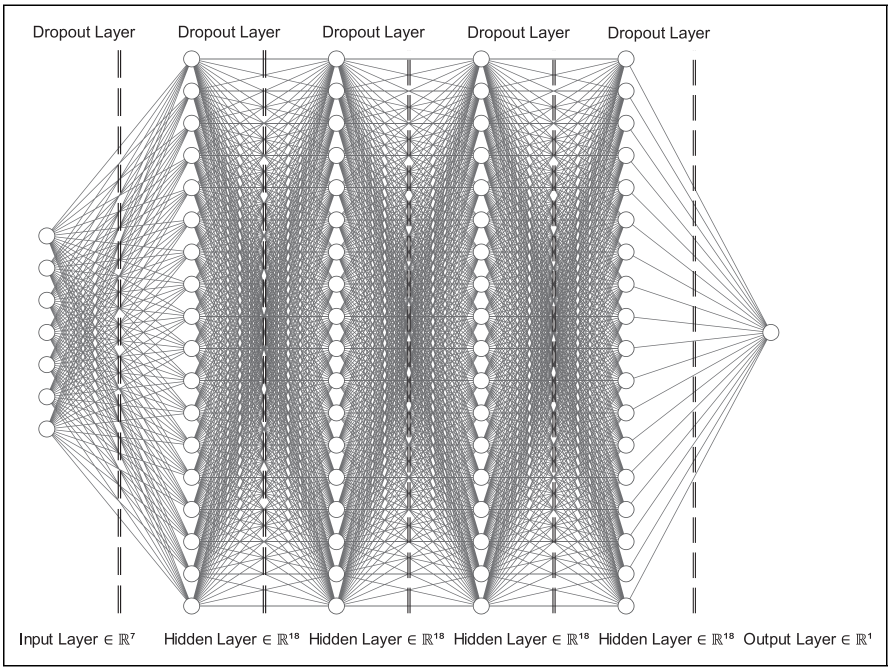

Figure 9. Optimised neural network structure generated from the hyperparameter optimisation scheme.

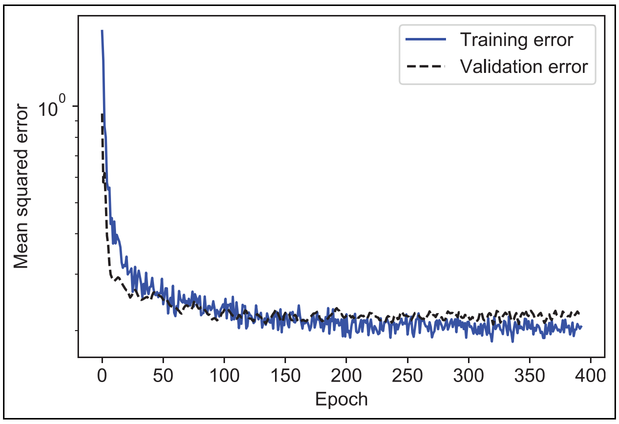

Figure 10. Convergence of the neural network model by reduction of RMS state of health prediction error with number of training epochs. Training and validation errors are well matched suggesting no over-fitting of the training data.

Using the sixfold cross-validation scheme, the RMS, MA and peak prediction errors for the baseline model were generated as a benchmark to compare with the performance of the optimised model. This comparison is summarised in Table 5. The results show that the hyperparameter optimisation provides a clear benefit over the baseline model, with significant improvements to RMS (0.403%) and MA (0.548%) error, while the lower standard deviation on these errors suggests that the optimised model generalises more consistently to unseen data. Little to no difference in peak error over the six trials was recorded, suggesting that while the optimised NN predictions are on average more accurate, there is little reduction in potential outlier predictions generated by the optimised network. This comparison is illustrated in Figure 11, showing graphically the distribution of predictions between the two models. A further comparison between the baseline model and the optimised model is presented in the variation of network accuracy with the number of training samples used in Figure 12. Each point represents the sixfold cross-validated RMS prediction error of each model averaged over 10 runs in total. From the graph, it is clear that the optimised model begins to

Table 5. Sixfold cross-validated RMS, mean absolute (MA) and peak prediction errors of state of health estimation for the baseline and optimised neural network model.

Trial (baseline)	1	2	3	4	5	6	Average
RMS error (SoH %)	2.132	1.813	2.820	2.575	1.706	2.111	2.193 ± 0.176
MA error (SoH %)	1.683	1.403	2.230	2.080	1.402	1.693	1.748 ± 0.140
Peak error (SoH %)	5.011	4.218	6.783	5.149	3.197	4.938	4.883 ± 0.483
RMS error (SoH %)	1.671	1.831	1.920	1.758	1.364	2.195	1.790 ± 0.112
MA error (SoH %)	1.147	1.341	1.172	1.143	1.016	1.385	1.200 ± 0.056
Peak error (SoH %)	4.104	5.286	6.141	4.098	3.680	6.007	4.886 ± 0.435

RMS: root mean square; SoH: state of health.

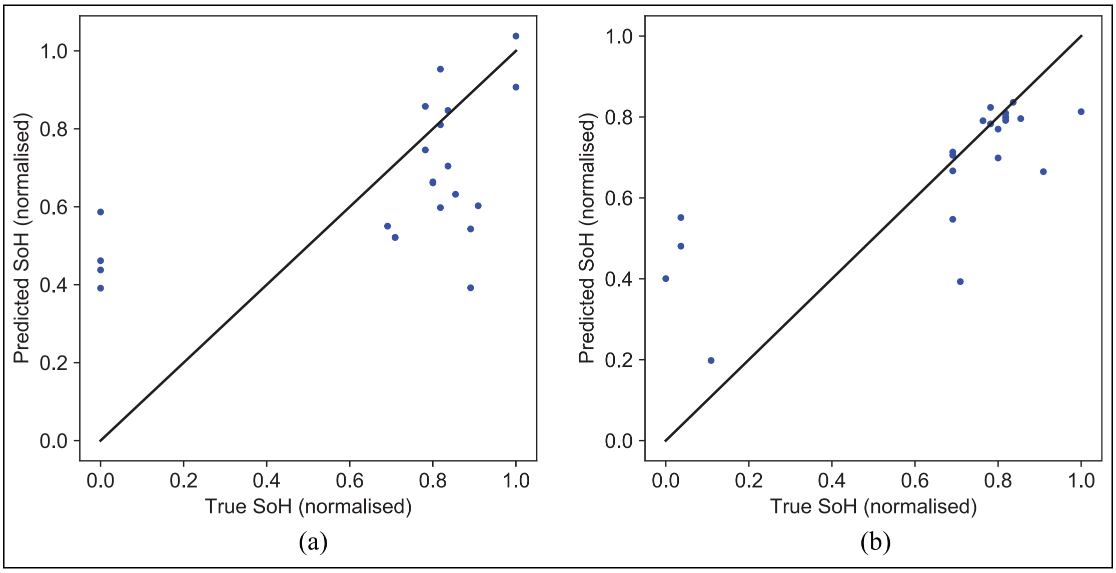

Figure 11. Distribution of predicted versus ground truth state of health values shown as a scatter plot for a single baseline and optimised model cross-validation trial, with RMS errors of 2.314% and 1.679%, respectively: (a) scatter plot for baseline model trial; (b) scatter plot for optimised model trial. The SoH values (range: 77%–85%) are normalised to the range 0–1 for clarity..

outperform the baseline for training datasets of greater than around 50 samples, with the cross-over point at 43 samples. Overall, this demonstrates the greater generalising power of the optimised model over the baseline.

It is noted that the additional model complexity introduced presents a considerable downside over the baseline model, leading to an increase in training and evaluation times. On the hardware used in this study, the training and evaluation times for the baseline NN were 0.925 ± 0.07 s and 0.023 ± 0.003 s, respectively. For the optimised model, this increases to 6.5 ± 0.7 s and 0.0617 ± 0.0007 s, respectively. In this case, there is mainly a negative impact on training times, with minimal absolute change in evaluation times. Even in the optimised case, the model training times are significantly reduced compared to a convolutional NN-based approach with ensemble learning (143.396 s)[18] of greater complexity; it should also be noted that the quoted time was obtained on considerably more powerful hardware than used in this study. On this basis, the increased level of complexity is therefore deemed acceptable in the scope of this work to improve prediction accuracy.

Optimised network evaluation

The distribution of predictions is an important factor for accurate SoH estimation. It is necessary for both sorting cells given a screening criterion, such as cells being above or below 80% of their original capacity, and for matching of cells of similar SoH that cells are sorted with high accuracy. This necessitates low SoH prediction error and low tendency towards over and under-estimation. Figure 13 presents the model predictions from a trial where the model performed well, achieving an RMS prediction error of 1.570%, and a less well-performing trial with 2.205%. The well-performing trial demonstrates that there is good agreement between the NN predictions and the respective ground truth values, with few outliers and a relatively uniform distribution of predictions in spite of the sparsity of the dataset towards lower SoH values. Results for the less well-performing model suggest that the model generalised well to much of the dataset, however in this case produced a number of outliers. The overall optimised NN performance corresponds to an average RMS prediction error of 1.790% (SoH) over sixfold cross-validation trials as shown in Table 5. In both cases, there is a tendency towards slight over-estimation of SoH towards lower 'true' SoH values; however, for

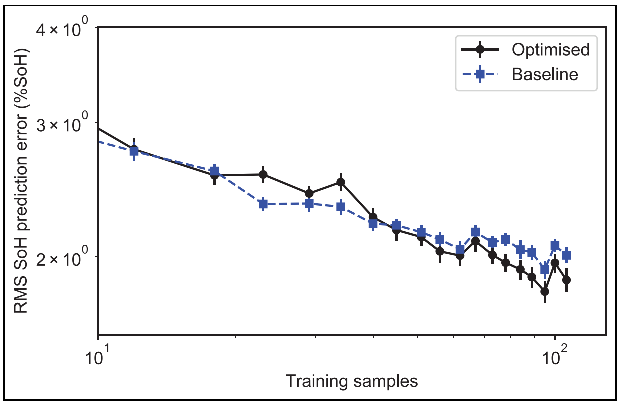

Figure 12. Variation of sixfold cross-validated RMS state of health prediction error for the baseline and hyperparameter optimised model with the number of training samples used.

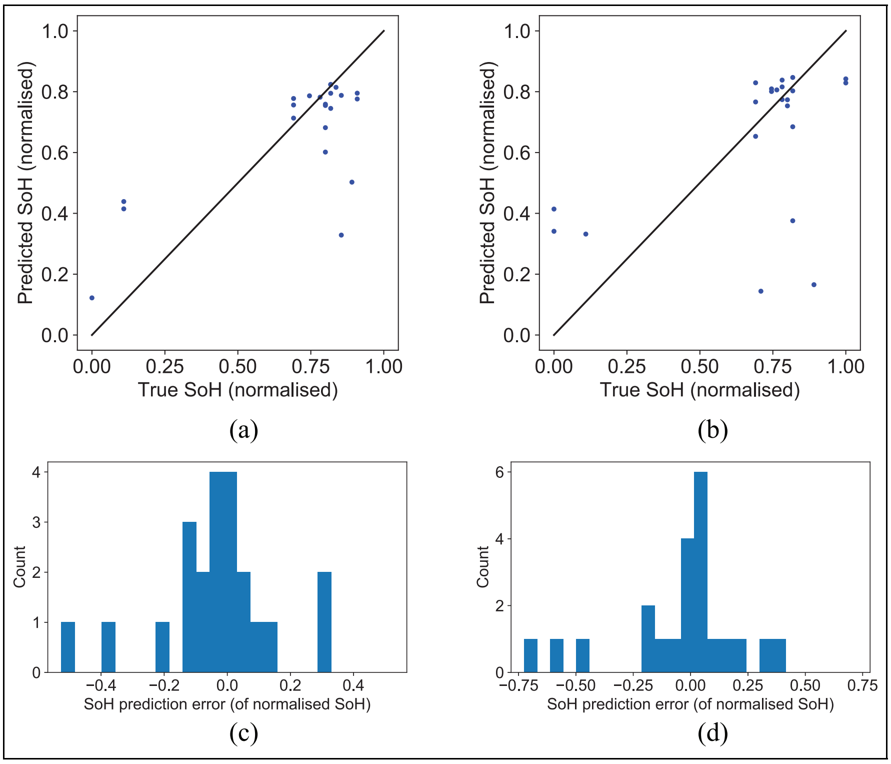

Figure 13. Distribution of predicted versus ground truth state of health values shown as a scatter plot and histogram for high- (RMS error: 1.570%) and low-performing (RMS error: 2.205%) model trials: (a) scatter plot for high-performing trial; (b) scatter plot for low-performing trial; (c) distribution of errors for high-performing trial; and (d) distribution of errors for low-performing trial. The SoH values (range: 77%–85%) are normalised to the range 0–1 for clarity..

Table 6. Comparison of RMS, mean absolute and peak prediction errors between this work, machine learning approaches covered by existing studies and the commonly used techniques – Gaussian process (GP) and random forest (RF) regression.

Method	RMS err. (SoH %)	MA err. (SoH %)	Peak err. (SoH %)	# training samples
Linear regression (R_{ct}, 60% SoC)[13]	6.780	5.911	14.3	26
ANN[16]	4.05	3.48	7.2	~40
GP regression[52]	2.681	2.353	7.431	106
ELM[15]	2.4	–	–	~520
RF (ET) regression[52]	2.092	1.779	7.123	106
This work (unmodified Randles)	2.091 ± 0.360	1.447 ± 0.345	6.641	106
This work	1.790 ± 0.112	1.200 ± 0.056	6.141	106
DCNN-ETL[18]	1.503	–	9.505	340 (+ 25,338 initial training)
RNN[12]	0.462	–	–	500

RMS: root mean square; SoH: state of health; MA: mean absolute; ELM: extreme learning machine; ANN: artificial neural network; DCNN-ETL: deep convolutional neural networks with ensemble learning and transfer learning; RNN: recurrent neural network.

the most part, the high and low SoH cells are clearly distinguished from each other.

Table 6 summarises the RMS, MA and peak errors of two alternative popular machine learning approaches for small datasets: GP and random forest (RF) ‘extra trees’ regression, using the implementations provided by Pedregosa et al.[52] to estimate SoH using the extracted ECM parameters in comparison with this work. Additionally shown are prediction errors for related SoH estimation schemes presented by previous works.[12,13,15,16,18]

For linear regression, the errors were obtained by application of linear regression of the charge transfer resistance for this work’s dataset as proposed by Wang et al.[13] in this case for data at 60% SoC. For the ELM approach in Densmore and Hanif,[15] the number of training samples is calculated based on the samples available in the open source NASA Ames dataset used. For the ANN approach in Yang et al.,[16] the values for RMS error and MA error are calculated from the published test dataset SoH prediction errors, while the number of samples is obtained based on the author quoted value of five cells used for training. The peak error is the maximum quoted error by each of these studies; for this work, it is the maximum error recorded over sixfold cross-validation as shown in Table 5, and provides an indication of the maximum error expected from the SoH estimation method in comparison with related works. As a further comparison, the cross-validation results from the optimised model using the original Randles circuit model introduced in Figure 2 are presented. This ECM describes the impedance data less accurately, increasing the uncertainty in the extracted parameters; this demonstrates how the model predictions are influenced by a suboptimal choice of ECM with additional error on the extracted parameters.

The results of cross-validation trials as shown in Table 6 suggest that a linear regression of the charge transfer resistance is insufficient in this case to accurately predict the battery SoH. The optimised NN model proposed in this work is shown to surpass the performance of well-established regression schemes for the dataset used, while also presenting a reasonable improvement of ~2.26% over a similar ECM parameter approach[16] for estimating battery SoH, even when considering the smaller dataset used. In this case, the similar performance of the model in this work to that of Yang et al.[16] demonstrates that an ECM approach based on EIS can be directly applied with an ANN model to estimate SoH reliably in spite of the uncertainty introduced by the SoC dependence and the fitting process for the values of extracted ECM parameters. This is corroborated by results for the optimised model presented in this work using the unmodified Randles ECM. Here, there is an increase in 0.301% in the model RMS error compared with the optimised model using the modified Randles circuit, which is most likely caused by the additional fitting error introduced, leading to a less informative set of SoH predictors. However, even in this case, the model still outperforms the original baseline model, RF (ET) and GP regression, even when these approaches are trained with the modified Randles circuit parameters, suggesting the model is able to reduce the influence of fitting error on the overall SoH prediction. Based on the variation of model performance with availability of training data established (Figure 12), it is likely that with a larger dataset of ~200 samples, the technique proposed reaches parity with the most performant NN approaches such as those by Shen et al.[18]

A principal limitation of this work is that the temperature dependence of impedance data has not been considered in this study, and therefore a larger training dataset would be required including temperature as a parameter to make the model robust to temperature changes, or measurements would need to be carried out in a climate-controlled environment. The former could be achieved either by including the temperature directly as a learnable parameter, as with SoC, or normalised to a standard state as proposed by Wang et al.[13] to address this limitation. There is also scope to further reduce the uncertainty inherent in application of non-linear least squares fitting of the raw impedance data imparted to the ECM parameter values obtained. This uncertainty can potentially be reduced by application of a parameter search algorithm, such as those applied by Wang et al.[13] and Tröltzsch et al.[27] Currently, this approach also requires an appropriate choice of ECM based on knowledge of the cell impedance response.

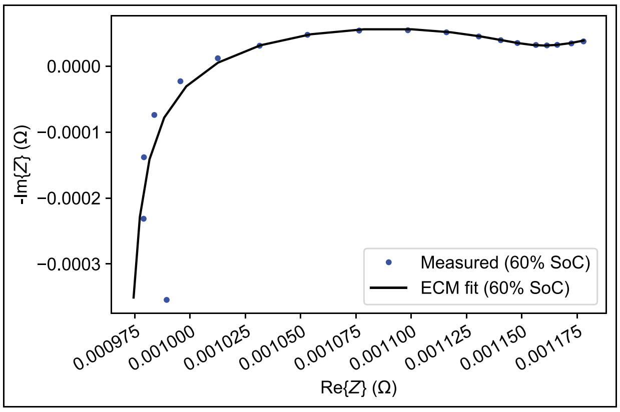

Figure 14. Fit to equivalent circuit model in Figure 4 with experimental impedance data obtained at 60% SoC, 25 °C over the red and white terminals of module 1 of 13, capacity 54.9 A h, limited to the frequency range 1–200 Hz.

Reduction of measurement times

The primary area of improvement afforded by an ECM parameter–based SoH estimation scheme is additional insight into the battery condition than made available by most SoH monitoring schemes.[6] Another area for potential improvement is improving measurement times associated with collection of impedance data to a level to achieve parity with previous related works such as Bonfitto et al.,[17] which operate on 60-s cell I–V profiles to predict SoH. To achieve this, it is possible to target specific frequencies corresponding to regions of interest in an impedance spectrum, such as the double-layer capacitive loop. This particular region of the spectrum in this case lies in the frequency range 1–200 Hz. Such schemes have previously been applied in time critical scenarios such as quality control of fresh batteries,[26] and represent a powerful tool for reduction of measurement times. As a guideline, given a minimum of six probing cycles at each frequency point[26] at six points per decade, it is estimated that measurement times could be reduced to as little as 30 s. To demonstrate this is feasible, fits to the same ECM were performed on the existing dataset using the reduced frequency range as presented in Figure 14, and the optimised model retrained on the extracted parameters.

The results of further cross-validation trials as summarised in Table 7 suggest that there is potential to greatly improve measurement times with only a small

Table 7. Sixfold cross-validated RMS, mean absolute and peak prediction errors of state of health estimation for the optimised neural network model using parameters extracted from a reduced frequency range.

Trial	1	2	3	4	5	6	Average
RMS error (SoH %)	2.468	2.104	1.893	2.247	1.233	1.750	1.949 ± 0.177
MA error (SoH %)	1.530	1.397	1.164	1.460	0.789	1.223	1.260 ± 0.110
Peak error (SoH %)	8.227	6.179	5.854	5.072	3.569	4.687	5.598 ± 0.647

RMS: root mean square; SoH: state of health; MA: mean absolute.

detriment (0.16%) to RMS prediction error. One area of improvement, however, is that the peak prediction error is significantly increased. It is possible that such errors could be reduced by employing ensemble learning techniques as with Shen et al.,[18] where the predictions of multiple models were combined to the benefit of accuracy. However, this was considered out of scope for the current work due the constraints of the project to maintain a level of model simplicity, as this further increases the required time to train and evaluate the model.

Conclusion

An NN model has been developed to estimate the SoH of 2P arrangements of high-power Lithium Manganese cells based on parameters extracted from impedance spectroscopy data by non-linear least squares fitting to a modified Randles ECM, using a library of impedance and capacity data extracted from 13 Nissan Leaf 2011 battery modules. Starting with a single hidden layer baseline model, an optimised NN was generated by a GP hyperparameter optimisation scheme, which was demonstrated to exceed the performance of the baseline model for training datasets of ~50 samples. The model cross-validated RMS, MA and peak SoH prediction errors of (1.790 ± 0.112)%, (1.200 ± 0.056)%, and 6.141%, respectively, were demonstrated to be competitive with alternative SoH estimation schemes and exceeds the performance of existing approaches based on extraction of ECM parameters. While the SoC dependence was successfully accounted for by the NN model proposed, a principal limitation of this work is that the temperature dependence of the battery impedance data has not been considered, which ultimately must either be controlled or accounted for by inclusion of temperature as an additional predictor for the SoH or normalisation to a standard state as proposed in previous works. To reduce the measurement times associated with the collection of impedance data, the model performance was assessed based on ECM parameters extracted from a reduced frequency range of 1–200 Hz associated with the capacitive impedance response of the cell. Re-evaluation of the NN model under this condition suggests that there is potential for measurement times to be reduced to as little as 30 s with limited (0.16%) increase in the RMS prediction error, but an increase in the peak prediction error to 8.227%.

Acknowledgements

The authors would like to thank our partners Dr Musbahu Muhammad, Dr Pierrot Attidekou and the team at Newcastle University for their collaboration and work on the dataset applied in this study.

Data availability statement

The data that support the findings of this study are openly available in Figshare with DOI (10.6084/m9.figshare.12227282).[53]

Declaration of conflicting interests

The author(s) declared no potential conflicts of interest with respect to the research, authorship, and/or publication of this article.

Funding

The author(s) disclosed receipt of the following financial support for the research, authorship, and/or publication of this article: This research was conducted as part of the project called 'Reuse and Recycling of Lithium-Ion Batteries' (RELIB). This work was supported by the Faraday Institution (grant number: FIRG005).

ORCID iD

Alireza Rastegarpanah https://orcid.org/0000-0003-4264-6857

References

1. Pinegar H and Smith Y. Recycling of end-of-life lithium ion batteries, part I: commercial processes. *J Sustain Metallurg* 2019; 5(3): 402–416.
2. Elwert T, Goldmann D, Römer F, et al. Current developments and challenges in the recycling of key components of (hybrid) electric vehicles. *Recycling* 2015; 1(1): 25–60.
3. Diekmann J, Hanisch C, Frobose L, et al. Ecological recycling of lithium-ion batteries from electric vehicles with focus on mechanical processes. *J Electrochem Soc* 2017; 164(1): A6184–A6191.

4. Tong S, Fung T, Klein M, et al. Demonstration of reusing electric vehicle battery for solar energy storage and demand side management. *J Energ Storage* 2017; 11: 200–210.
5. Braco E, Martín IS, Sanchis P, et al. Characterization and capacity dispersion of lithium-ion second-life batteries from electric vehicles. In: *2019 IEEE international conference on environment and electrical engineering and 2019 IEEE industrial and commercial power systems Europe (EEEIC/I CPS Europe)*, Genova, 11–14 June 2019, pp.1–6. New York: IEEE.
6. Li Y, Liu K, Foley A, et al. Data-driven health estimation and lifetime prediction of lithium-ion batteries: a review. *Renew Sustain Energ Rev* 2019; 113: 109254.
7. Muhammad M, Ahmeid M, Attidekou PS, et al. Assessment of spent EV batteries for second-life application. In: *2019 IEEE 4th international future energy electronics conference (IFEEC)*, Singapore, 25–28 November 2019, pp.325–329. New York: IEEE.
8. Andre D, Meiler M, Steiner K, et al. Characterization of high-power lithium-ion batteries by electrochemical impedance spectroscopy. I. Experimental investigation. *J Power Sourc* 2011; 196(12): 5334–5341.
9. Waag W, Käbitz S and Sauer D. Experimental investigation of the lithium-ion battery impedance characteristic at various conditions and aging states and its influence on the application. *Appl Energ* 2013; 102: 885–897.
10. Stiaszny B, Ziegler J, Krauß E, et al. Electrochemical characterization and post-mortem analysis of aged LiMn2O4-Li(Ni0.5Mn0.3Co 0.2)O2/graphite lithium ion batteries. Part I: cycle aging. *J Power Sourc* 2014; 251: 439–450.
11. Zhu J, Dewi Darma M, Knapp M, et al. Investigation of lithium-ion battery degradation mechanisms by combining differential voltage analysis and alternating current impedance. *J Power Sourc* 2020; 448: 227575.
12. Eddahech A, Briat O, Bertrand N, et al. Behavior and state-of-health monitoring of Li-ion batteries using impedance spectroscopy and recurrent neural networks. *Int J Electr Power Energ Syst* 2012; 42(1): 487–494.
13. Wang X, Wei X and Dai H. Estimation of state of health of lithium-ion batteries based on charge transfer resistance considering different temperature and state of charge. *J Energ Storage* 2019; 21: 618–631.
14. Leng Y, Ge S, Marple D, et al. Electrochemical cycle-life characterization of high energy lithium-ion cells with thick Li(Ni0.6Mn0.2Co0.2)O2 and graphite electrodes. *J Electrochem Soc* 2017; 164(6): A1037–A1049.
15. Densmore A and Hanif M. Modeling the condition of lithium ion batteries using the extreme learning machine. In: *2016 IEEE PES PowerAfrica conference*, Livingstone, 28 June–3 July 2016, pp.184–188. New York: IEEE.
16. Yang D, Wang Y, Pan R, et al. A neural network based state-of-health estimation of lithium-ion battery in electric vehicles. *Energy Procedia* 2017; 105: 2059–2064.
17. Bonfitto A, Ezemobi E, Amati N, et al. State of health estimation of lithium batteries for automotive applications with artificial neural networks. In: *AEIT international conference of electrical and electronic technologies for automotive (AEIT AUTOMOTIVE)*, Torino, 2–4 July 2019, pp.1–5. New York: IEEE.
18. Shen S, Sadoughi M, Li M, et al. Deep convolutional neural networks with ensemble learning and transfer learning for capacity estimation of lithium-ion batteries. *Appl Energ* 2020; 260: 114296.
19. Qu S, Kang Y, Gu P, et al. A fast online state of health estimation method for lithium-ion batteries based on incremental capacity analysis. *Energies* 2019; 12(17): 1–11.
20. Gismero A, Schaltz E and Stroe DI. Recursive state of charge and state of health estimation method for lithium-ion batteries based on coulomb counting and open circuit voltage. *Energies* 2020; 13(7): 1811.
21. Park J, Lee M, Kim G, et al. Integrated approach based on dual extended Kalman filter and multivariate autoregressive model for predicting battery capacity using health indicator and SOC/SOH. *Energies* 2020; 13(9): 2138.
22. Gholizadeh M and Yazdizadeh A. Systematic mixed adaptive observer and EKF approach to estimate SOC and SOH of lithium–ion battery. *IET Electr Syst Transp* 2020; 10(2): 135–143.
23. Perez A, Quintero V, Jaramillo F, et al. Characterization of the degradation process of lithium-ion batteries when discharged at different current rates. *Proc IMechE, Part I: J Systems and Control Engineering* 2018; 232(8): 1075–1089.
24. Sarmah S, Kalita P, Garg A, et al. A review of state of health estimation of energy storage systems: challenges and possible solutions for futuristic applications of Li-ion battery packs in electric vehicles. *J Electrochem Energ Convers Storage* 2019; 16(4): 42987.
25. Chang L, Wang C, Zhang C, et al. A novel fast capacity estimation method based on current curves of parallel-connected cells for retired lithium-ion batteries in second-use applications. *J Power Sourc* 2020; 459: 227901.
26. Lambert S, Armstrong M, Attidekou P, et al. Rapid nondestructive-testing technique for in-line quality control of Li-ion batteries. *IEEE T Ind Electron* 2017; 64(5): 4017–4026.
27. Tröltzsch U, Kanoun O and Tränkler HR. Characterizing aging effects of lithium ion batteries by impedance spectroscopy. *Electrochimica Acta* 2006; 51(8–9): 1664–1672.
28. Pastor-Fernández C, Uddin K, Chouchelamane G, et al. A comparison between electrochemical impedance spectroscopy and incremental capacity-differential voltage as Li-ion diagnostic techniques to identify and quantify the effects of degradation modes within battery management systems. *J Power Sourc* 2017; 360: 301–318.
29. Schindler S and Danzer M. A novel mechanistic modeling framework for analysis of electrode balancing and degradation modes in commercial lithium-ion cells. *J Power Sourc* 2017; 343: 226–236.
30. Barai A, Uddin K, Dubarry M, et al. A comparison of methodologies for the non-invasive characterisation of commercial Li-ion cells. *Prog Energ Combust Sci* 2019; 72: 1–31.
31. Xie Y, Li J and Yuan C. Mathematical modeling of the electrochemical impedance spectroscopy in lithium ion battery cycling. *Electrochimica Acta* 2014; 127: 266–275.
32. Liu L and Zhu M. Modeling of SEI layer growth and electrochemical impedance spectroscopy response using a thermal-electrochemical model of Li-ion batteries. *ECS Trans* 2014; 61(27): 43–61.
33. Attidekou P, Lambert S, Armstrong M, et al. A study of 40 ah lithium ion batteries at zero percent state of charge

as a function of temperature. *J Power Sourc* 2014; 269: 694–703.

34. Oldenburger M, Bedürftig B, Gruhle A, et al. Investigation of the low frequency Warburg impedance of Li-ion cells by frequency domain measurements. *J Energ Storage* 2019; 21: 272–280.
35. Orazem ME and Tribollet B. Electrochemical impedance spectroscopy. In: Orazem MA and Tribollet B. (eds) *Electrochemical society series*. Hoboken, NJ: John Wiley & Sons, 2008, pp.63–69.
36. Ahmeid M, Muhammad M, Milojevic Z, et al. The energy loss due to interconnections in paralleled cell configurations of lithium-ion batteries in electric vehicles. In: *2019 IEEE 4th international future energy electronics conference (IFEEC)*, Singapore, 25–28 November 2019, pp.1–4. New York: IEEE.
37. Li X, Zhang W and Ding Q. Deep learning-based remaining useful life estimation of bearings using multi-scale feature extraction. *Reliab Eng Syst Safe* 2019; 182: 208–218.
38. Li X, Zhang W, Ding Q, et al. Multi-layer domain adaptation method for rolling bearing fault diagnosis. *Signal Pr* 2019; 157: 180–197.
39. Jiao M, Wang D and Qiu J. A GRU-RNN based momentum optimized algorithm for SOC estimation. *J Power Sourc* 2020; 459: 228051.
40. Mamo T and Wang FK. Long short-term memory with attention mechanism for state of charge estimation of lithium-ion batteries. *IEEE Access* 2020; 8: 94140–94151.
41. Kim J, Yu J, Kim M, et al. Estimation of Li-ion battery state of health based on multilayer perceptron: as an EV application. *IFAC-PapersOnline* 2018; 51(28): 392–397.
42. Kwon SJ, Han D, Choi J, et al. Remaining-useful-life prediction via multiple linear regression and recurrent neural network reflecting degradation information of 20Ah $LiNi_xMn_yCo_{1-x-y}O2$ pouch cell. *J Electroanal Chem* 2020; 858: 113729.
43. Li P, Zhang Z, Xiong Q, et al. State-of-health estimation and remaining useful life prediction for the lithium-ion battery based on a variant long short term memory neural network. *J Power Sourc* 2020; 459: 228069.
44. Liu C, Tan J, Shi H, et al. Lithium-ion cell screening with convolutional neural networks based on two-step time-series clustering and hybrid resampling for imbalanced data. *IEEE Access* 2018; 6: 59001–59014.
45. Jabeur Telmoudi A, Soltani M, Chaouech L, et al. Parameter estimation of nonlinear systems using a robust possibilistic c-regression model algorithm. *Proc IMechE, Part I: J Systems and Control Engineering* 2020; 234(1): 134–143.
46. Telmoudi A, Soltani M, Ben Belgacem Y, et al. Modeling and state of health estimation of nickel–metal hydride battery using an EPSO-based fuzzy c-regression model. *Soft Comput* 2020; 24(10): 7265–7279.
47. Newville M, Stensitzki T, Allen D, et al. Non-linear least-squares minimization and curve-fitting for python, 2015, https://lmfit.github.io/lmfit-py/
48. Abadi M, Agarwal A, Barham P, et al. TensorFlow: large-scale machine learning on heterogeneous systems (arXiv preprint arXiv:1603.04467), 2016, https://www.tensorflow.org/.Software available from tensorflow.org
49. Kingma D and Ba J. Adam: a method for stochastic optimization. In: *International conference on learning representations*, San Diego, CA, 7–9 May 2014. Ithaca, NY: arXiv.org.
50. Hastie T, Tibshirani R and Friedman JH. *The elements of statistical learning: data mining, inference, and prediction*. 2nd ed. New York: Springer, 2009.
51. Chollet F. *Deep learning with Python*. 1st ed. New York: Manning Publications, 2018.
52. Pedregosa F, Varoquaux G, Gramfort A, et al. Scikit-learn: machine learning in python. *J Mach Learn Res* 2011; 12: 2825–2830.
53. Rastegarpanah A. *Data library: electrochemical impedance spectroscopy dataset and neural network code*. 1st ed. Figshare, 2020. DOI: 10.6084/m9.figshare.12227282

Appendix 1

Extracted ECM parameters

Table 8. Table of ECM parameters extracted from impedance measurements of modules 1–13 in the data library used in this study at 60% SoC, 25 °C with corresponding SoH.[53]

Battery arrangement	R_e (Ω)	R_{ct} (Ω)	Q_{dl} (Ω^{-1} $s^{n_{dl}}$)	n_{dl}
Module 1 RW	$9.69 \times 10^{-4} \pm 6.85 \times 10^{-6}$	$1.77 \times 10^{-4} \pm 8.81 \times 10^{-6}$	35.3 ± 8.33	0.852 ± 0.0480
Module 1 BW	$1.08 \times 10^{-3} \pm 1.42 \times 10^{-5}$	$1.86 \times 10^{-4} \pm 1.89 \times 10^{-5}$	28.5 ± 14.99	0.911 ± 0.1054
Module 2 RW	$1.00 \times 10^{-3} \pm 1.11 \times 10^{-5}$	$2.06 \times 10^{-4} \pm 1.46 \times 10^{-5}$	34.2 ± 11.64	0.842 ± 0.0693
Module 2 BW	$1.07 \times 10^{-3} \pm 1.25 \times 10^{-5}$	$1.71 \times 10^{-4} \pm 1.66 \times 10^{-5}$	28.8 ± 14.79	0.923 ± 0.1021
Module 3 RW	$9.62 \times 10^{-4} \pm 9.84 \times 10^{-6}$	$2.11 \times 10^{-4} \pm 1.26 \times 10^{-5}$	35.0 ± 9.43	0.822 ± 0.0557
Module 3 BW	$1.05 \times 10^{-3} \pm 1.21 \times 10^{-5}$	$1.79 \times 10^{-4} \pm 1.58 \times 10^{-5}$	30.2 ± 13.54	0.899 ± 0.0903
Module 4 RW	$9.92 \times 10^{-4} \pm 1.09 \times 10^{-5}$	$2.06 \times 10^{-4} \pm 1.42 \times 10^{-5}$	32.6 ± 10.79	0.845 ± 0.0672
Module 4 BW	$1.08 \times 10^{-3} \pm 1.47 \times 10^{-5}$	$1.88 \times 10^{-4} \pm 1.96 \times 10^{-5}$	32.4 ± 17.12	0.898 ± 0.1076
Module 5 RW	$9.75 \times 10^{-4} \pm 1.11 \times 10^{-5}$	$2.12 \times 10^{-4} \pm 1.42 \times 10^{-5}$	34.3 ± 10.25	0.821 ± 0.0619
Module 5 BW	$1.08 \times 10^{-3} \pm 1.56 \times 10^{-5}$	$1.96 \times 10^{-4} \pm 2.06 \times 10^{-5}$	32.9 ± 17.24	0.877 ± 0.1066
Module 6 RW	$1.00 \times 10^{-3} \pm 1.10 \times 10^{-5}$	$2.02 \times 10^{-4} \pm 1.46 \times 10^{-5}$	31.3 ± 11.27	0.872 ± 0.0728
Module 6 BW	$1.10 \times 10^{-3} \pm 1.85 \times 10^{-5}$	$2.01 \times 10^{-4} \pm 2.41 \times 10^{-5}$	30.3 ± 17.80	0.880 ± 0.1197
Module 7 RW	$9.86 \times 10^{-4} \pm 1.01 \times 10^{-5}$	$2.08 \times 10^{-4} \pm 1.33 \times 10^{-5}$	32.3 ± 10.01	0.850 ± 0.0629
Module 7 BW	$1.10 \times 10^{-3} \pm 1.85 \times 10^{-5}$	$2.09 \times 10^{-4} \pm 2.45 \times 10^{-5}$	32.6 ± 18.73	0.870 ± 0.1178
Module 8 RW	$9.33 \times 10^{-4} \pm 7.74 \times 10^{-6}$	$2.09 \times 10^{-4} \pm 9.84 \times 10^{-6}$	35.2 ± 7.28	0.817 ± 0.0430

(continued)

Table 8. Continued

Battery arrangement	R_e (Ω)	R_{ct} (Ω)	Q_{dl} ($\Omega^{-1}\ s^{n_{dl}}$)	n_{dl}
Module 8 BW	$1.09 \times 10^{-3} \pm 1.56 \times 10^{-5}$	$1.79 \times 10^{-4} \pm 2.02 \times 10^{-5}$	31.7 ± 17.73	0.895 ± 0.1136
Module 9 RW	$1.02 \times 10^{-3} \pm 1.71 \times 10^{-5}$	$2.33 \times 10^{-4} \pm 2.22 \times 10^{-5}$	37.9 ± 15.93	0.797 ± 0.0881
Module 9 BW	$1.08 \times 10^{-3} \pm 1.71 \times 10^{-5}$	$2.12 \times 10^{-4} \pm 2.28 \times 10^{-5}$	33.5 ± 17.84	0.857 ± 0.1086
Module 10 RW	$1.03 \times 10^{-3} \pm 1.51 \times 10^{-5}$	$2.25 \times 10^{-4} \pm 1.98 \times 10^{-5}$	31.8 ± 13.47	0.840 ± 0.0864
Module 10 BW	$1.11 \times 10^{-3} \pm 2.09 \times 10^{-5}$	$2.17 \times 10^{-4} \pm 2.74 \times 10^{-5}$	30.7 ± 18.71	0.867 ± 0.1252
Module 11 RW	$9.84 \times 10^{-4} \pm 9.09 \times 10^{-6}$	$1.94 \times 10^{-4} \pm 1.20 \times 10^{-5}$	34.7 ± 10.50	0.858 ± 0.0615
Module 11 BW	$1.08 \times 10^{-3} \pm 1.24 \times 10^{-5}$	$1.65 \times 10^{-4} \pm 1.66 \times 10^{-5}$	35.4 ± 18.56	0.914 ± 0.1063
Module 12 RW	$9.64 \times 10^{-4} \pm 8.16 \times 10^{-6}$	$1.86 \times 10^{-4} \pm 1.05 \times 10^{-5}$	34.5 ± 9.13	0.847 ± 0.0539
Module 12 BW	$1.03 \times 10^{-3} \pm 1.00 \times 10^{-5}$	$1.63 \times 10^{-4} \pm 1.31 \times 10^{-5}$	34.0 ± 13.72	0.897 ± 0.0814
Module 13 RW	$9.62 \times 10^{-4} \pm 7.62 \times 10^{-6}$	$1.92 \times 10^{-4} \pm 1.01 \times 10^{-5}$	35.5 ± 9.09	0.852 ± 0.0519
Module 13 BW	$1.03 \times 10^{-3} \pm 9.67 \times 10^{-6}$	$1.54 \times 10^{-4} \pm 1.26 \times 10^{-5}$	38.6 ± 15.71	0.887 ± 0.0827

Battery arrangement	R_W (Ω)	T_W (s)	L (H)	SoH
Module 1 RW	$1.08 \times 10^{-3} \pm 2.61 \times 10^{-4}$	92.5 ± 41.4	$5.84 \times 10^{-8} \pm 1.35 \times 10^{-9}$	0.845
Module 1 BW	$1.09 \times 10^{-3} \pm 7.31 \times 10^{-4}$	102.9 ± 129.4	$8.93 \times 10^{-8} \pm 3.41 \times 10^{-9}$	0.854
Module 2 RW	$1.12 \times 10^{-3} \pm 4.96 \times 10^{-4}$	101.1 ± 83.9	$2.14 \times 10^{-8} \pm 2.11 \times 10^{-9}$	0.837
Module 2 BW	$1.09 \times 10^{-3} \pm 6.43 \times 10^{-4}$	100.8 ± 111.0	$7.15 \times 10^{-8} \pm 2.91 \times 10^{-9}$	0.842
Module 3 RW	$1.14 \times 10^{-3} \pm 3.91 \times 10^{-4}$	99.7 ± 64.0	$6.89 \times 10^{-8} \pm 1.92 \times 10^{-9}$	0.842
Module 3 BW	$1.09 \times 10^{-3} \pm 5.76 \times 10^{-4}$	100.6 ± 99.5	$9.23 \times 10^{-8} \pm 2.68 \times 10^{-9}$	0.846
Module 4 RW	$1.14 \times 10^{-3} \pm 4.82 \times 10^{-4}$	101.1 ± 80.0	$3.40 \times 10^{-8} \pm 1.96 \times 10^{-9}$	0.837
Module 4 BW	$1.10 \times 10^{-3} \pm 7.58 \times 10^{-4}$	103.8 ± 134.1	$1.08 \times 10^{-7} \pm 3.47 \times 10^{-9}$	0.840
Module 5 RW	$1.13 \times 10^{-3} \pm 4.34 \times 10^{-4}$	100.4 ± 71.8	$7.48 \times 10^{-8} \pm 2.11 \times 10^{-9}$	0.838
Module 5 BW	$1.09 \times 10^{-3} \pm 7.61 \times 10^{-4}$	103.7 ± 134.8	$8.81 \times 10^{-8} \pm 3.49 \times 10^{-9}$	0.835
Module 6 RW	$1.13 \times 10^{-3} \pm 5.35 \times 10^{-4}$	101.9 ± 90.2	$6.95 \times 10^{-8} \pm 2.50 \times 10^{-9}$	0.838
Module 6 BW	$1.06 \times 10^{-3} \pm 8.57 \times 10^{-4}$	103.6 ± 155.6	$1.20 \times 10^{-7} \pm 4.07 \times 10^{-9}$	0.838
Module 7 RW	$1.12 \times 10^{-3} \pm 4.53 \times 10^{-4}$	99.8 ± 75.5	$4.24 \times 10^{-8} \pm 1.95 \times 10^{-9}$	0.838
Module 7 BW	$1.08 \times 10^{-3} \pm 8.96 \times 10^{-4}$	104.7 ± 161.9	$1.03 \times 10^{-7} \pm 4.16 \times 10^{-9}$	0.832
Module 8 RW	$1.13 \times 10^{-3} \pm 2.88 \times 10^{-4}$	97.3 ± 46.0	$7.58 \times 10^{-8} \pm 1.47 \times 10^{-9}$	0.829
Module 8 BW	$1.08 \times 10^{-3} \pm 7.28 \times 10^{-4}$	102.6 ± 129.7	$1.32 \times 10^{-7} \pm 3.68 \times 10^{-9}$	0.828
Module 9 RW	$1.10 \times 10^{-3} \pm 6.84 \times 10^{-4}$	102.9 ± 119.0	$3.91 \times 10^{-8} \pm 3.25 \times 10^{-9}$	0.834
Module 9 BW	$1.10 \times 10^{-3} \pm 8.41 \times 10^{-4}$	104.8 ± 149.4	$4.20 \times 10^{-8} \pm 3.42 \times 10^{-9}$	0.832
Module 10 RW	$1.12 \times 10^{-3} \pm 6.96 \times 10^{-4}$	104.2 ± 120.9	$3.16 \times 10^{-8} \pm 3.17 \times 10^{-9}$	0.835
Module 10 BW	$1.07 \times 10^{-3} \pm 9.66 \times 10^{-4}$	104.7 ± 176.8	$1.19 \times 10^{-7} \pm 4.74 \times 10^{-9}$	0.835
Module 11 RW	$1.14 \times 10^{-3} \pm 4.19 \times 10^{-4}$	99.6 ± 68.5	$5.49 \times 10^{-8} \pm 1.77 \times 10^{-9}$	0.828
Module 11 BW	$1.09 \times 10^{-3} \pm 6.59 \times 10^{-4}$	102.2 ± 115.4	$8.97 \times 10^{-8} \pm 3.10 \times 10^{-9}$	0.828
Module 12 RW	$1.19 \times 10^{-3} \pm 3.57 \times 10^{-4}$	102.0 ± 57.3	$6.72 \times 10^{-8} \pm 1.64 \times 10^{-9}$	0.772
Module 12 BW	$1.15 \times 10^{-3} \pm 4.93 \times 10^{-4}$	102.3 ± 82.4	$9.71 \times 10^{-8} \pm 2.36 \times 10^{-9}$	0.778
Module 13 RW	$1.19 \times 10^{-3} \pm 3.68 \times 10^{-4}$	102.4 ± 59.5	$3.36 \times 10^{-8} \pm 1.41 \times 10^{-9}$	0.769
Module 13 BW	$1.17 \times 10^{-3} \pm 4.79 \times 10^{-4}$	103.4 ± 79.2	$9.67 \times 10^{-8} \pm 2.25 \times 10^{-9}$	0.769

ECM: equivalent circuit model; SoC: state of charge; SoH: state of health.

The battery arrangements RW and BW correspond to measurements across the red and white and black and white terminals on the Nissan Leaf 2011 module, respectively.